Journal of Materials Chemistry A

PAPER

View Article Online
View Journal

Cite this: DOI: 10.1039/c7ta06790a

Controlling and correlating the effect of grain size with the mechanical and electrochemical properties of $Li_7La_3Zr_2O_{12}$ solid-state electrolyte†

Asma Sharafi, [a] Catherine G. Haslam, [a] Robert D. Kerns,[b] Jeff Wolfenstine[c] and Jeff Sakamoto *[a]

Received 1st August 2017
Accepted 15th September 2017

DOI: 10.1039/c7ta06790a

rsc.li/materials-a

$Li_7La_3Zr_2O_{12}$ (LLZO) solid-state electrolyte is garnering interest due to its potential to enable solid-state batteries (SSBs) using metallic Li anodes. However, Li metal propagates along LLZO grain boundaries at high Li plating current densities (above the critical current density, CCD). In the present study, we examined whether microstructural aspects, such as grain size, could influence mechanical and electrochemical properties thereby affecting the CCD. A unique densification technique (heating between 1100 and 1300 °C) was used to control grain size. Electron backscatter diffraction determined that the grain size and the misorientation angle varied from 5 to 600 μm and 20 to 40°, respectively. Vickers indentation was used to characterize the mechanical properties and revealed that hardness decreased (9.9–6.8 GPa) with increasing grain size, but the fracture toughness was invariant (0.6 MPa $m^{-1/2}$) at grain sizes ≥40 μm. DC and AC techniques were used to measure and correlate the CCD with grain size and showed that the CCD increased with increasing grain size achieving a maximum of 0.6 mA cm^{-2}. We believe the implications of this work could be far-reaching in that they represent a significant step towards understanding the mechanism(s) that control the stability of the Li–LLZO interface and a rational approach to increase the CCD in SSBs.

1. Introduction

Li-ion batteries (LIBs) are a promising technology to meet near-term vehicle electrification needs, however achieving wide-scale adoption of electric vehicles will require a step increase in energy density (>1000 W h l^{-1}).[1–3] It is known that dramatically increasing energy density is possible by replacing conventional state-of-the-art anodes with metallic Li; but, stabilizing the Li–electrolyte interface has been a difficult challenge to overcome.[2] Thus, there is a great-unmet need for strategies to stabilize the metallic Li interface during cycling, especially at high plating rates. One approach involves the integration of solid-state electrolytes (SSEs) with metallic Li. The garnet-type SSE, with the nominal formula $Li_7La_3Zr_2O_{12}$ (LLZO), is promising, because it simultaneously satisfies several key performance criteria such as chemical and electrochemical stability against metallic Li and high ionic conductivity (1 mS cm^{-1} at room temperature).[4–9] Despite satisfying these and other performance characteristics, numerous barriers remain. We believe that the maximum Li plating rate is one of the primary challenges preventing the maturation of LLZO membrane technology. We and others have observed that Li metal propagates into LLZO at or above current densities ranging from 0.05 to 0.2 mA cm^{-2}.[10–15] Although perhaps not directly related to crystalline materials, it has been suggested that the SSE shear modulus and the fracture toughness are important factors that affect the onset and propagation of alkali metals through SSEs, respectively.[16–18] Furthermore, in a recent study by E. J. Cheng *et al.* it was determined that Li metal propagates along grain boundaries in polycrystalline LLZO when the critical current density (CCD) is exceeded, (CCD is defined as the current density at and above which Li metal propagates through a SSE).[19] Thus, it was hypothesized that one strategy to increase the CCD is to reduce the area fraction of grain boundaries by increasing the grain size.[19] While there are several hypotheses that could help elucidate the phenomena that govern the CCD, to date, none have been validated for solid-state alkali metal–SSE interfaces or more specifically the Li–LLZO interface. It follows that the purpose of this study was multi-fold. One goal was to understand grain growth kinetics to allow for the fabrication of LLZO with a wide grain size range. Another goal was to correlate the effects of grain size with the mechanical and electrochemical properties such as the CCD. Finally, the overarching goal of this

[a]Department of Mechanical Engineering, University of Michigan, 2350 Hayward Street, Ann Arbor, Michigan 48109, USA. E-mail: jeffsaka@umich.edu

[b]Michigan Center of Materials Characterization, University of Michigan, 2800 Plymouth Road, Ann Arbor, Michigan 48109, USA

[c]RDRL-SED-C, Army Research Laboratory, 2800 Powder Mill Road, Adelphi, Maryland 20783, USA

† Electronic supplementary information (ESI) available: Histograms and probability distribution curves, projected grain boundary trajectory. See DOI: 10.1039/c7ta06790a

work was to better understand the underpinning mechanisms that govern the stability of the Li–LLZO interface.

A concerted suite of aspects was studied comprising ceramic processing, materials characterization, mechanical property measurements, and electrochemical analyses. Polycrystalline LLZO was densified using hot-pressing and annealing. Based on the processing conditions, the average LLZO grain size ranged between 5 and 600 μm. LLZO microstructures were characterized using standard materials characterization techniques as well as electron backscatter diffraction (EBSD) to obtain grain size, grain orientation, and grain boundary misorientation angle statistics. EBSD was used to analyse the grain growth mechanism and grain growth rate as a function of processing conditions. Vickers indentation was used to determine hardness and fracture toughness as a function of grain size. Finally, direct current (DC) and electrochemical impedance spectroscopy (EIS) were used to evaluate the CCD as a function of grain size. Taken together, these data were used to correlate the effects of LLZO grain size and mechanical properties on controlling the CCD.

2. Experimental

2.1. Powder synthesis and pellet processing of solid-state electrolyte

Cubic Al-doped LLZO with the nominal composition of $Li_{6.25}Al_{0.25}La_3Zr_2O_{12}$ was prepared using a solid-state synthetic technique. This composition was chosen due to its high ionic conductivity and stability against metallic Li.[8,9,20–22] Li_2CO_3 (99.0%, Alfa Aesar), $La(OH)_3$ (99.95%, Alfa Aesar), ZrO_2 (99.9%, Inframat Advanced Materials), and Al_2O_3 (99.9%, Mager Scientific) precursors were combined in stoichiometric quantities and dry-milled for 4 h at 350 rpm in a planetary ball mill (Retsch GmbH). A 5 wt% excess Li_2CO_3 precursor was used to compensate for Li loss during calcination. The resulting mixed powder was pressed into pellets with a diameter of 25.4 mm using a stainless-steel die (MTI Corporation) at 10 MPa. The cold-pressed pellets were placed on a MgO boat (Ozark Technical Ceramics) and calcined at 1000 °C for 4 h in a tube furnace (STF 15/180, Carbolite LTD) under flowing dry air (Cryogenic gases, <3 ppm moisture). The calcined pellets were ground into powder using a mortar and pestle and passed through a 75 μm sieve.

For hot-pressing, 6 g of powder was cold-pressed into a pellet with 12.7 mm diameter using a stainless-steel die at 62 MPa. The green density of the pellet was measured by dividing the mass by the measured volume (geometrical density). The relative density (RD%) was defined as the ratio of the geometric density and the theoretical density (5.17 g cm^{-3}) with relative densities of green pellets ranging from 52 to 55%. The green pellet was placed in a graphite die then hot-pressed using a custom rapid induction hot-pressing (RIHP) technique at a uniaxial 62 MPa pressure for 1 h under a flowing argon atmosphere. The microstructural evolution and grain growth were controlled by changing the hot-pressing temperature: 1100 °C, 1200 °C, 1250 °C, and 1300 °C. We will refer to these samples as HP-1100 °C, HP-1200 °C, HP-1250 °C, and HP-1300 °C. Increasing hot-pressing temperature >1300 °C resulted in significant Li loss, thus the maximum hot-pressing temperature was 1300 °C. After hot-pressing, specimens were cut into pellets (1.1 ± 0.2 mm thickness) using a diamond saw (11-2180, Buehler). An alternative approach with a combination of hot-pressing and annealing was used to further grow grains. For this approach, HP-1100 °C pellets were embedded into LLZO mother powder in a MgO boat and annealed in a tube furnace under flowing argon for 50 h at 1300 °C (A-1300 °C). The heating and cooling rates were 4 °C min^{-1}.

The pellets were ground by mechanical grinding using 400 grit sandpaper (Norton Corporation) and a polishing fixture (Model 150, South Bay Technology) to achieve parallel faces. Next, the pellets were ground using 600 grit and 1200 grit sandpaper followed by polishing (AutoMet 250, Buehler) using 15 μm, 6 μm, 1 μm, and 0.5 μm diamond polishing compounds (LECO Corporation) with a glycol based diamond extender (LECO Corporation). For all steps, 10 N force was applied to each pellet during polishing and the head and base were rotated at 210 rpm and 60 rpm, respectively. For all mechanical property and electrochemical characterizations, the final polishing step was 0.5 μm. For electron backscatter diffraction (EBSD) analysis, additional polishing was done using a colloidal silica suspension (Mager Scientific) with 0.03 μm particle size for 1 h and then washed with deionized water to remove the silica from the surface. The final polishing step was done immediately before EBSD analysis to minimize surface contamination and ensure that high quality electron backscatter patterns are obtained.

2.2. Materials characterization

2.2.1 X-ray diffraction (XRD). XRD (MiniFlex 600, Rigaku) was used to characterize the crystalline phases present in the LLZO powder and LLZO pellets after hot-pressing and annealing. Samples were spun during XRD to ensure diffraction from multiple grains, especially for pellets with larger (>40 μm) grain sizes. Spectra were collected from 15 to 65° 2θ, at a rate of 4.5° min^{-1} in 0.02° increments using CuKα radiation operating at 40 kV and 15 mA. Rietveld refinement and Jade 2010 software (Version 5.0.0, Materials Data Inc.) were used to determine and quantify the weight fraction of phases present. The following reference crystallographic information files were used: cubic LLZO (PDF# 04-018-3158), $La_2Zr_2O_7$ (PDF# 01-070-5602), and $La_{0.28}Zr_{0.72}O_{1.86}$ (PDF# 04-002-7939).

2.2.2 Scanning electron microscopy (SEM) and electron backscatter diffraction (EBSD). SEM was performed on the polished surfaces of LLZO pellets using a FEI Nova 200 lab dual beam at 10 kV accelerating voltage and 5 mm working distance. EBSD measurements were conducted using an EDAX detector and TEAM software on a Tescan MIRA3 SEM. The microscope was operated at an accelerating voltage of 30 kV and a working distance of 20 mm. For EBSD analysis, the pellets were tilted at 70° toward the EBSD detector. A step size of 5 μm was used to construct EBSD maps. The backscatter diffraction patterns were fit to a custom material profile using information from PDF# 04-018-3158. The collected data were analysed using EDAX OIM

data collection software. The datasets were refined by dilating the grains in a single iteration. Grain dilation is an iterative OIM data-cleaning method, which assigns an orientation to a point that does not belong to any grains. Using this method, the orientations of neighboring points are obtained and the orientation of a cleaning point is assigned to the orientation of most neighboring points.

2.2.3 Mechanical properties. The Vickers hardness (H) of hot-pressed and annealed pellets was measured using a Vickers hardness tester (HM122V/K Series 810 Micro, Mitutoyo Corporation). Before indentation, the indenter was calibrated using a steel hardness block (Hardness Test Block HMV 700 HV, Mitutoyo Corporation). The Vickers hardness tests were conducted at a load of 0.098 N for an indentation time of 10 s. The load was chosen specifically for each sample to reduce microcracking. The average hardness of each specimen was determined by using ten indentations. No indentations were placed closer than 1000 μm from the pellet edge, and a separation distance of at least 150 μm was maintained between adjacent indentations. The H values were determined by eqn (1):[23]

$$H = \frac{1.854P}{d^2} \quad (1)$$

where P is the applied load, and d is the length of the diagonal of the Vickers indentation impression.

The fracture toughness (K_{IC}) of hot-pressed and annealed pellets was determined using the indentation technique on a Vickers indenter. The applied load was 0.196 N, chosen to produce measurable crack lengths with a crack radius about 2–3 times larger than the half diagonal for all the measurements. In all cases, the dwell time was 10 s and ten indents were made per pellet. Crack lengths were determined using an optical microscope and confirmed by SEM (Nova 200 NanoLab, FEI) images right after indentations were made. The K_{IC} was calculated using eqn (2):[24]

$$K_{IC} = \xi\left(\frac{E}{H}\right)^{0.5}\frac{P}{{c_0}^{1.5}} \quad (2)$$

where ξ is a material-independent constant (0.016), E is the Young's modulus (150 GPa),[25,26] H is the hardness, c_0 is the crack length, and P is the applied load. The loads for H and K_{IC} measurements were kept constant for all pellets to eliminate the effect of load as a variable.

2.3. Electrochemical characterization

Electrochemical impedance spectroscopy (EIS) was performed on the hot-pressed and annealed LLZO pellets to determine the room temperature ionic conductivity. Gold electrodes were sputter coated on both sides of each pellet using a sputter coater (Desk V, Denton Vacuum) with a gold target (99.99%, Angstrom Engineering). EIS was performed at 25 °C from 1 Hz to 7 MHz with a 100 mV perturbation amplitude using a potentiostat/galvanostat (VMP300, Bio-Logic) and EC-Lab V10.44 software. The thickness and diameter of each pellet was used to normalize the collected data for conductivity calculations.

DC electrochemical measurements were performed to determine the maximum tolerable current density (critical current density, CCD). Prior to Li–LLZO–Li cell assembly, polished LLZO pellets were heat-treated in a muffle furnace (KSL-1100X, MTI Corporation) inside an argon-filled glovebox (0.1 ppm O_2 and 1 ppm H_2O) to reduce surface contamination that forms during air exposure. Pellets were placed on a MgO boat inside the furnace and heated to 400 °C for 3 h using 4 °C min^{-1} as the heating and the cooling rate. Li foil (Alfa Aesar) was scraped with a stainless-steel spatula to remove the surface contamination layer before being used. Solid-state symmetric cells were assembled by placing heat-treated LLZO pellets between two Li electrodes. A load frame was used to apply a constant uniaxial pressure (3.5 MPa). EIS measurements were conducted on the assembled cell in the load frame. The cell was removed from the load frame and preconditioned by heating to 175 °C for 12 h to improve contact between metallic Li and LLZO as demonstrated by Sharafi *et al.*[10] Each cycling test has been repeated three times to confirm reproducibility. After cooling to room temperature, another EIS spectrum was collected and normalized to the contact area between Li and LLZO (area = 1.26 cm^2). An equivalent circuit model was used to interpret the data and to determine the contribution of each resistive component to the total cell impedance. In this model, a combination of a resistor and a capacitor in parallel are used to represent each component in the cell. Thus, three parallel combinations were used in the model representing the bulk (Z_{bulk}), the grain boundary (Z_{gb}), and the Li–LLZO interfacial ($Z_{Li-LLZO}$) impedance as shown schematically in Fig. 8a. Ideal capacitors were replaced with constant phase elements (CPE) to account for the non-idealized behavior and dispersion of the time constant. The ideality of the CPE is represented by the coefficient α ($\alpha = 1$ shows that the component is behaving as an ideal capacitor). The Q values for the CPE should be on the order of 10^{-12} F, 10^{-8} F, and 10^{-6} F for bulk, grain boundaries and the Li–LLZO interface, respectively.[27,28] The data fitting and circuit modeling was done with a software package EC-Lab V10.44. To determine the effect of grain size on CCD, Li–LLZO–Li symmetric cells were cycled between 0.01 and 1 mA cm^{-2} at room temperature under a constant uniaxial pressure (3.5 MPa). Cycling was continued until a sudden drop in polarization voltage occurred, indicating short-circuiting of the cell. EIS was performed after DC cycling to confirm the short-circuiting.

3. Results

3.1. Crystallographic and microstructural analysis of cubic $Li_7La_3Zr_2O_{12}$ (LLZO)

3.1.1 Crystal structure. X-ray diffraction (XRD) was used to characterize the crystal structure of LLZO powder and LLZO pellets hot-pressed between 1100 and 1300 °C (Fig. 1). The calcined powder and all pellets primarily were single-phase cubic LLZO (space group $Ia\bar{3}d$). However, a low concentration of pyrochlore (<3 vol%) was present in the HP-1200 °C and HP-1250 °C pellets. Previous reports have shown that pyrochlore can form due to Li loss during calcination and/or densification

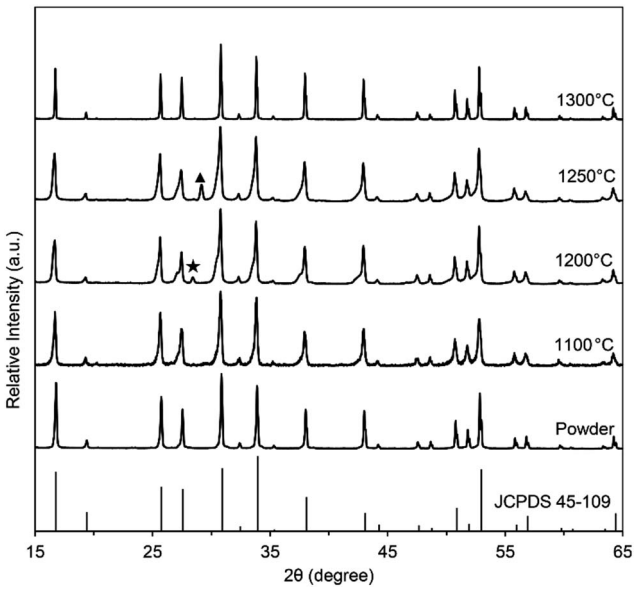

Fig. 1 XRD patterns of LLZO calcined powder and pellets hot-pressed between 1100 and 1300 °C. Secondary phases: ▲ ($La_2Zr_2O_7$) and ★ ($La_{0.28}Zr_{0.72}O_{1.86}$). JCPDS file # 45-109 was used for cubic garnet.

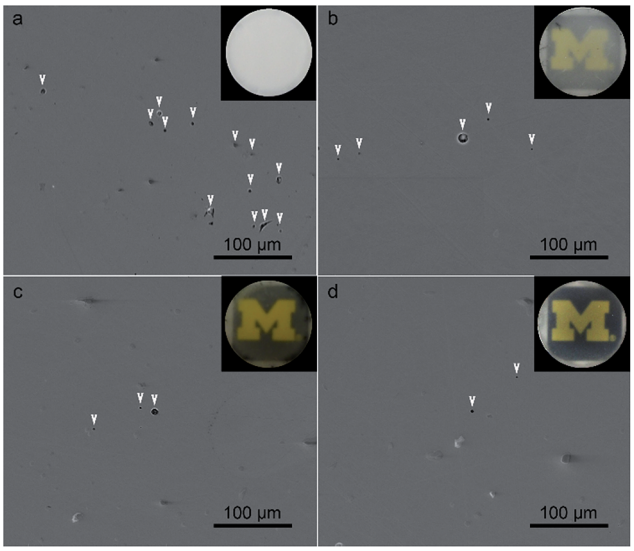

Fig. 2 Secondary electron SEM images of polished LLZO pellets: (a) HP-1100 °C, (b) HP-1200 °C, (c) HP-1250 °C, and (d) HP-1300 °C. Arrows indicate pores. Insets are optical images of hot-pressed LLZO pellets (12.7 mm diameter).

at high temperatures.[20,29] HP-1300 °C did not contain pyrochlore possibly due to the higher densification rate compared to the HP-1200 °C and HP-1250 °C pellets. For example, it has been shown that as the densification rate increases, the pore collapse accelerates, and thus the propensity for Li loss through sublimation diminishes.[21,22] Since the amount of secondary phases (3 vol%) in the hot-pressed pellets is small, their effects on the mechanical and electrochemical properties will be neglected and the results attributed only to single-phase cubic LLZO.

3.1.2 Microstructure. The relative density increased with increasing hot-pressing temperature, ranging between 96.0 ± 0.5% and 99.4 ± 0.5% for the pellets hot-pressed between 1100 and 1300 °C, respectively (Table 1). To further analyse the microstructural evolution as a function of hot-pressing temperature, scanning electron microscopy (SEM) analysis was conducted on polished surfaces (Fig. 2). Additionally, optical images of the hot-pressed pellets are shown in Fig. 2. From Fig. 2, a trend between the volume fraction of porosity and optical transparency was apparent. As the hot-pressing temperature increased, both the porosity and grain boundary area decreased resulting in higher relative density and transparency. Typically, transparency in dense polycrystalline ceramics is achieved by eliminating defects such as porosity and/or secondary phases with different indices of refraction[34] by increasing the densification temperature and/or time.[30,31] Thus, the observations made in this study are consistent with what is commonly observed when processing transparent polycrystalline ceramics. It is worth noting that the high relative densities achieved for all pellets likely eliminated the porosity as a variable in the mechanical properties and electrochemical characterization analyses.

3.2. Grain growth

Two methods were used to grow grains; (1) increasing the hot-pressing temperature and (2) hot-pressing at 1100 °C followed by annealing without pressure at 1300 °C for 50 h. To characterize the grain growth behavior, EBSD analysis was conducted after hot-pressing between 1100 and 1300 °C and annealing for

Table 1 Summary of the LLZO microstructural, mechanical, and electrochemical properties

	Microstructural properties				Mechanical properties		Electrochemical properties	
Pellet	Phase purity	Relative density (%)	d_{ave} (μm)	Misorientation angle (°)	H (GPa)	K_{IC} (MPa m$^{-1/2}$)	σ_{total} (mS cm^{-1})	CCD (mA cm^{-2})
HP-1100 °C	Cubic LLZO	96.0 ± 0.5	5 ± 2	20	9.88 ± 0.49	0.82 ± 0.07	0.46	0.3
HP-1200 °C	3 vol% pyrochlore	97.7 ± 0.5	40 ± 13	35	8.05 ± 0.52	0.61 ± 0.05	0.52	0.4
HP-1250 °C	1 vol% pyrochlore	98.1 ± 0.5	60 ± 20	40	7.74 ± 0.46	0.60 ± 0.06	0.54	0.4
HP-1300 °C	Cubic LLZO	99.4 ± 0.5	80 ± 20	40	7.42 ± 0.48	0.61 ± 0.04	0.56	0.5
A-1300 °C	Cubic LLZO	99.4 ± 0.5	600 ± 200	41	6.80 ± 0.49	0.60 ± 0.05	0.57	0.6

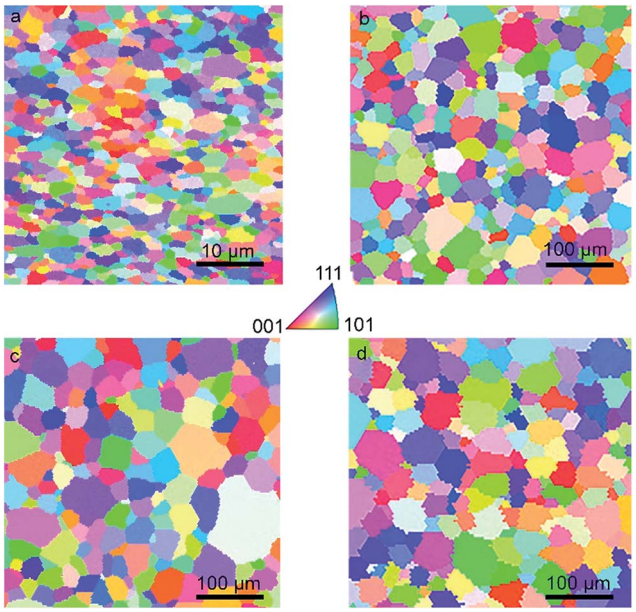

Fig. 3 EBSD grain orientation maps of LLZO pellets: (a) HP-1100 °C, (b) HP-1200 °C, (c) HP-1250 °C and (d) HP-1300 °C. The triangle in the centre correlates colour with crystallographic orientations.

50 h (Fig. 3 and 4b). The average grain size was determined using histograms and grain size probability distribution curves obtained from EBSD grain orientation maps (Fig. S1 and S2†). From the EBSD orientation maps in Fig. 3, it was apparent that the average grain size increased with increasing hot-pressing temperature. Table 1 summarizes the average grain size as a function of hot-pressing temperature. Increasing the hot-pressing temperature to >1300 °C resulted in significant Li loss; hence the maximum hot-pressing temperature was limited to 1300 °C. To further amplify the effects of grain size on the mechanical and electrochemical properties, an alternative grain growth approach was used, which involved annealing the HP-1100 °C LLZO at 1300 °C for 50 h (A-1300 °C). This approach resulted in significant grain growth with an average grain size of 600 ± 200 μm (Fig. 4b, and S2†). To better understand the grain growth phenomenon, detailed EBSD analysis was conducted to correlate the effects of temperature, grain boundary curvature, and grain boundary misorientation.

3.2.1 Effect of temperature. It was shown that the grain size increases with increasing hot-pressing temperature (Fig. 5a). Based on previous studies, it has been observed that grain growth is highly temperature dependent and typically increases with increasing temperature.[32–34] The relationship between grain size and temperature can be expressed by eqn (3):

$$d^n - d_0{}^n = k_0 t \exp\left(-\frac{Q}{RT}\right) \quad (3)$$

where d is the average grain size at a certain time (t), d_0 is the initial grain size, n is the grain growth exponent, Q is the activation energy for grain growth, R is the gas constant, T is the absolute temperature, and k_0 is an empirically derived proportionality constant. To determine the dominant grain growth mechanism and the ion that controls the grain growth rate, $\ln(d^n - d_0^n)$ was plotted *versus* $1/T$ using $n = 2$ and $n = 3$ and $t =$ 1 h for all temperatures. It was determined that $n = 2$ gave the best fit with $R^2 = 0.96$ (Fig. 5b). An n value equal to 2 is usually associated with normal grain growth with no secondary phases, impurities, or pores that could impede grain boundary mobility.[35–37] In contrast, $n = 3$ is typically associated with grain boundaries that drag secondary phases, impurities, or pores.[38,39] The n value equal to 2 is in agreement with previous transmission electron microscopy results for hot-pressed LLZO, which revealed the absence of secondary phases or impurities along grain boundaries or triple junctions.[20,40] In addition, since the LLZO tested in this study is of high relative density, pore drag is not expected to control grain growth. The activation energy for grain growth was determined from the slope of the line in Fig. 5b. The slope of the line yields an activation energy of 560 kJ mol^{-1}. It is well known that the rate-controlling species for grain growth of a ceramic is controlled by the slowest moving ion through the lattice or along the grain boundaries.[41,42] For LLZO, it is expected that La ions, which occupy the dodecahedral sites because of their large size, should be the rate-controlling species. Thus, the activation energy value of 560 kJ mol^{-1} should be correlated with La diffusion in LLZO. At present, no activation energy values for diffusion of any of the species in LLZO except for Li exist. However, for another material with the same garnet structure as LLZO, yttrium aluminium garnet (YAG), lattice diffusion data exist for the diffusion of rare-earth elements (La, Nd, Dy and Yb) which occupy the dodecahedral sites and Ga, which occupies the tetrahedral and octahedral sites in YAG.[43] The activation energies for the diffusion range between 540 and 603 kJ mol^{-1} for La, Nd, Dy and Yb, while the activation energy for Ga diffusion is lower, 404 kJ mol^{-1}. For the case of other materials with the garnet structure, yttrium iron garnet (YIG), activation energies for lattice diffusion of Y (dodecahedral site) and Fe (tetrahedral and octahedral sites) are 502 and 362 kJ mol^{-1}, respectively.[43] A comparison of the activation energy for grain growth of LLZO with cation diffusion data for YAG and YIG would suggest that the grain growth of LLZO is controlled by La lattice diffusion. However, in another study, it was observed that the activation energy for grain boundary diffusion of Yb in YAG was 530 kJ mol^{-1}, while that for lattice diffusion of Yb in YAG was 560 kJ mol^{-1}.[14] In this study, the activation energies for diffusion of the dodecahedral ion in the lattice and along the grain boundary are similar. Hence, to conclusively confirm that the grain growth of LLZO is controlled by La diffusion, cation (La, Zr) diffusion in LLZO through the lattice and along grain boundaries is needed.

3.2.2 Effect of grain boundary curvature. To better understand the effect of grain boundary curvature on grain growth kinetics, EBSD orientation maps were analysed (Fig. 3). From Fig. 3 several observations can be made. First, the grains can be categorized into three types: (type I) grains with six sides, which have straight boundaries, (type II) grains with less than six sides, which have concave grain boundaries (when observed from the centre of the grain), and (type III) grains with more than six sides, which have both concave and convex grain

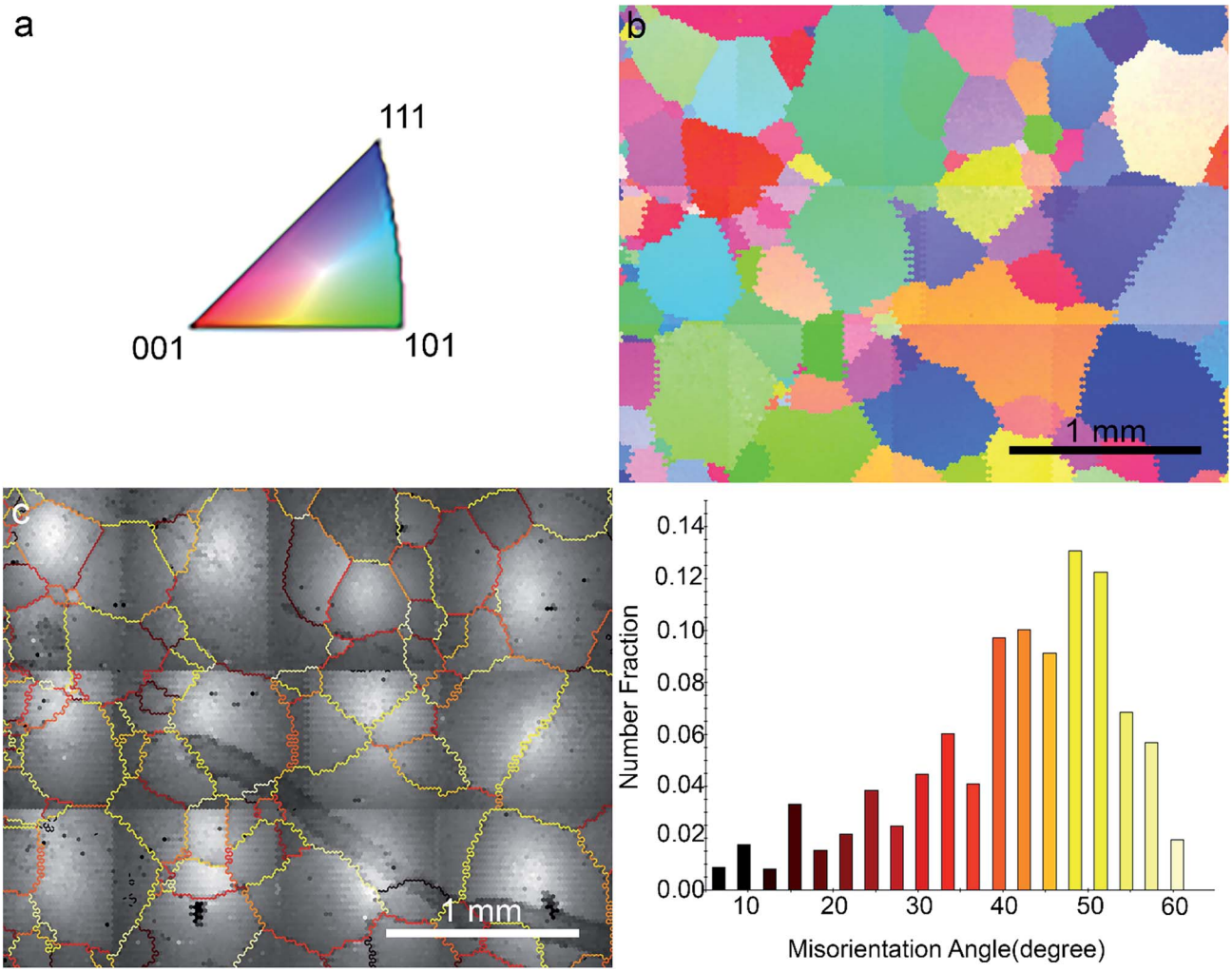

Fig. 4 (a) The triangle correlates color with crystallographic orientations, (b) EBSD grain orientation map, and (c) grain boundary misorientation angle map and histogram of an A-1300 °C LLZO pellet.

boundaries. Second, the hot-pressing temperature affects the microstructure. For example, the lower hot-pressing temperature (HP-1100 °C) resulted in grains with less than six sides and concave grain boundaries, while higher hot-pressing temperatures ($T \geq 1200$ °C) resulted in a higher fraction of grains with more than six sides and convex grain boundaries. Third, when hot-pressing at $T \geq 1200$ °C, the type III grains were typically surrounded by type II grains. De Jonghe *et al.* have shown that the grain boundary trajectory and mass transport during grain growth is controlled by chemical potential gradients related to the curvature of grain boundaries;[44] *i.e.* the atoms under a convex surface have a higher chemical potential than the atoms under a concave surface.[32,44,45] The Gibbs–Thomson equation (eqn (4)) correlates the chemical potential gradient $\Delta\mu_{gb}$ with grain boundary curvature:[32,44]

$$\Delta\mu_{gb} = \gamma_{gb}\Omega_{MX}k \quad (4)$$

where γ_{gb} is the grain boundary energy, Ω_{MX} is the volume of a formula unit, and k is the radius of curvature. The difference in the chemical potential energy across the grain boundary is what moves the grain boundary away from its centre and is the driving force for grain growth. Based on eqn (4), the type I grains with six sides and flat grain boundaries are stable and immobile, while grains with more than six sides with a positive curvature tend to grow at the expense of the smaller grains that have fewer than six sides and negative curvature. Thus, the larger grain size in LLZO pellets hot-pressed at $T \geq 1200$ °C can be attributed to the presence of more type III grains. Furthermore, the presence of curved grain boundaries in the microstructure of LLZO pellets reveals the potential for more grain growth upon holding time at high temperature. This phenomenon was confirmed by annealing LLZO after hot-pressing which exhibited a significant increase in grain size (600 μm). For better clarification, Fig. S3† shows the direction of grain boundary migration during grain growth.

3.2.3 Effect of grain boundary misorientation angle. To further examine the effect of grain boundary morphology on grain growth, the influence of the grain boundary misorientation angle was investigated. The grain boundary misorientation

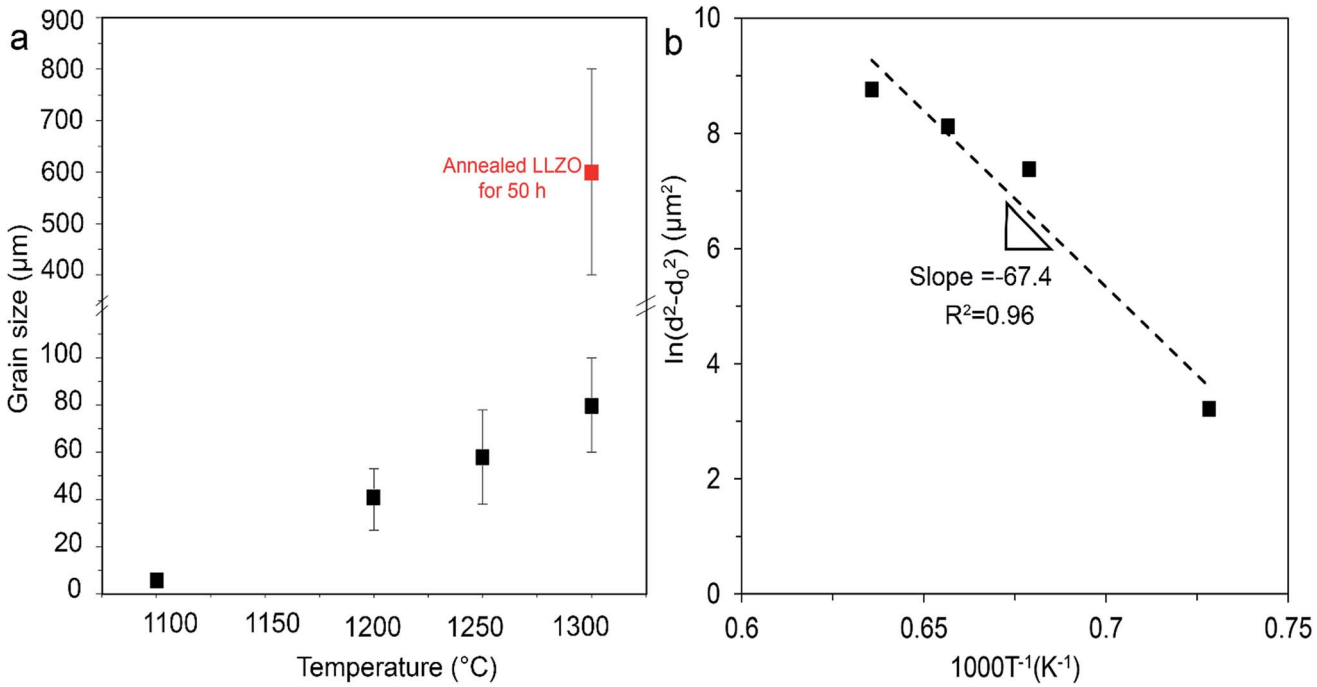

Fig. 5 LLZO grain growth data: (a) grain size as a function of hot-pressing temperature and (b) temperature dependence of grain growth. The experimental values are compared to the predictions made using eqn (3) for the grain growth mechanism.

angle maps and histograms of LLZO pellets hot-pressed at different temperatures are shown in Fig. 6. The same analysis was conducted on A-1300 °C (Fig. 4c). From Fig. 6 and 4c, several observations can be made. First, a wide range of misorientation angles between 0 and 65° were observed in all LLZO pellets. Second, there is a clear difference in the fraction of low to high misorientation angles comparing the HP-1100 °C, HP-1200 °C, HP-1250 °C, HP-1300 °C and A-1300 °C LLZO pellets. The average misorientation angles calculated from the histograms in Fig. 6 and 4c are listed in Table 1. It is apparent that the processing conditions affected the average misorientation angles. For example, the HP-1100 °C LLZO pellet had a higher fraction of low misorientation angles (<20°), while the LLZO pellets hot-pressed at $T \geq 1200$ °C and A-1300 °C had a higher fraction of boundaries with >35° misorientation angles. It has been shown by Barrett *et al.* that the degree of grain boundary misorientation is one of the primary factors influencing grain boundary mobility in polycrystalline Al; *i.e.* the higher the misorientation angle, the higher the grain boundary mobility, and hence the higher the grain growth rate.[46] It was shown that grain boundary mobility was negligible for grain boundaries with misorientation angles <15–20° whereas grain boundary mobility increased with higher misorientation angles.[47,48] In a related study, it was shown that the highest grain growth rate occurred when the misorientation angle was ≥40°.[49–53] Turning back to this study, the EBSD analysis corroborates the general trend between the grain boundary misorientation angle and the grain size. The LLZO pellets with the larger average grain size exhibited higher misorientation angles, especially when hot-pressing at $T \geq$ 1200 °C and in the A-1300 °C pellet. For example, all pellets but HP-1100 °C, had grain boundary misorientation angles between 35° and 40°, while the HP-1100 °C LLZO pellet had an average misorientation angle of 20°.

The effect of LLZO processing conditions on the grain size was studied to understand the phenomena that govern grain growth kinetics. It was determined that the processing temperature, grain boundary curvature, and grain boundary misorientation angle are important factors in controlling grain growth in LLZO. Moreover, the activation energy for grain growth and grain growth exponent revealed that hot-pressed LLZO exhibited normal grain growth, rate-limited by La diffusion. We believe that an understanding of grain growth will facilitate future efforts to integrate LLZO into SSBs, specifically regarding mechanical integrity and electrochemical performance as is discussed in subsequent sections.

3.3. Mechanical property characterization

3.3.1 Hardness. Vickers indentation was used to correlate hardness (H) with LLZO grain size (Fig. 7a). From Fig. 7a it can be observed that the hardness decreased from 9.88 ± 0.49 GPa to 6.86 ± 0.49 GPa as the average grain size increases from 5 μm to 600 μm, respectively. The HP-1100 °C H value for the 5 μm grain size pellet agrees with the H value measured by Kim *et al.* (9.1 ± 0.1 GPa) on hot-pressed LLZO with the same composition and similar grain size.[54] The H was correlated with the grain size (Fig. 7b) using the Hall–Petch relationship shown below, eqn (5):[55]

$$H = H_0 + K_H d^{-1/2} \quad (5)$$

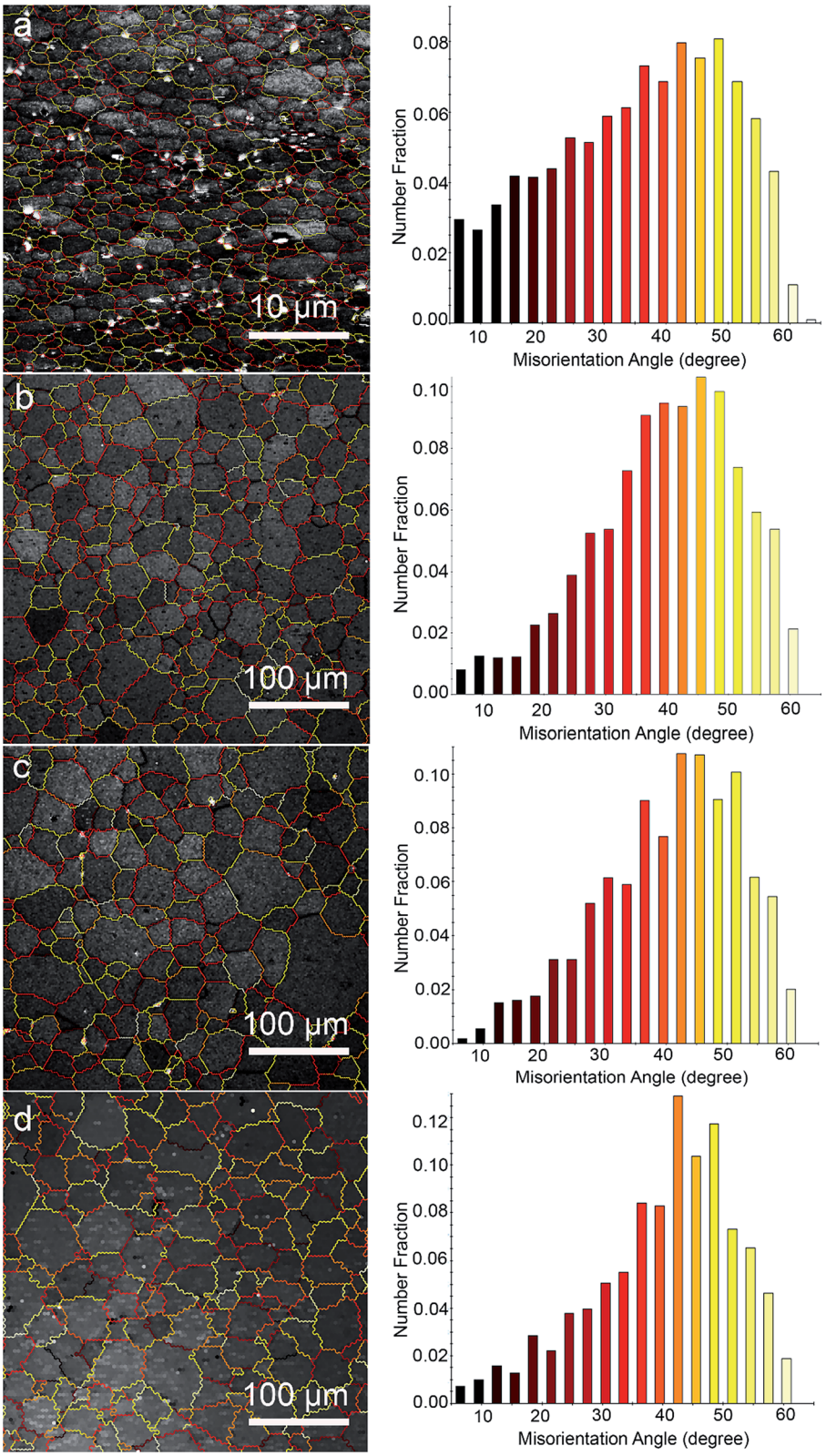

Fig. 6 Grain boundary misorientation angle maps and histograms of LLZO pellets: (a) HP-1100 °C, (b) HP-1200 °C, (c) HP-1250 °C, and (d) HP-1300 °C.

where d is the grain diameter, H_0 is the ordinate axis intercept corresponding to the hardness of a single crystal, and K_H is the slope of the straight line drawn through the data and corresponds to a material strengthening constant. Plotting the data from this study using eqn (5) gives the relationship: $H = 6.80 + 6.93d^{-1/2}$ with a R^2 value equal to 0.98. The high R^2 value

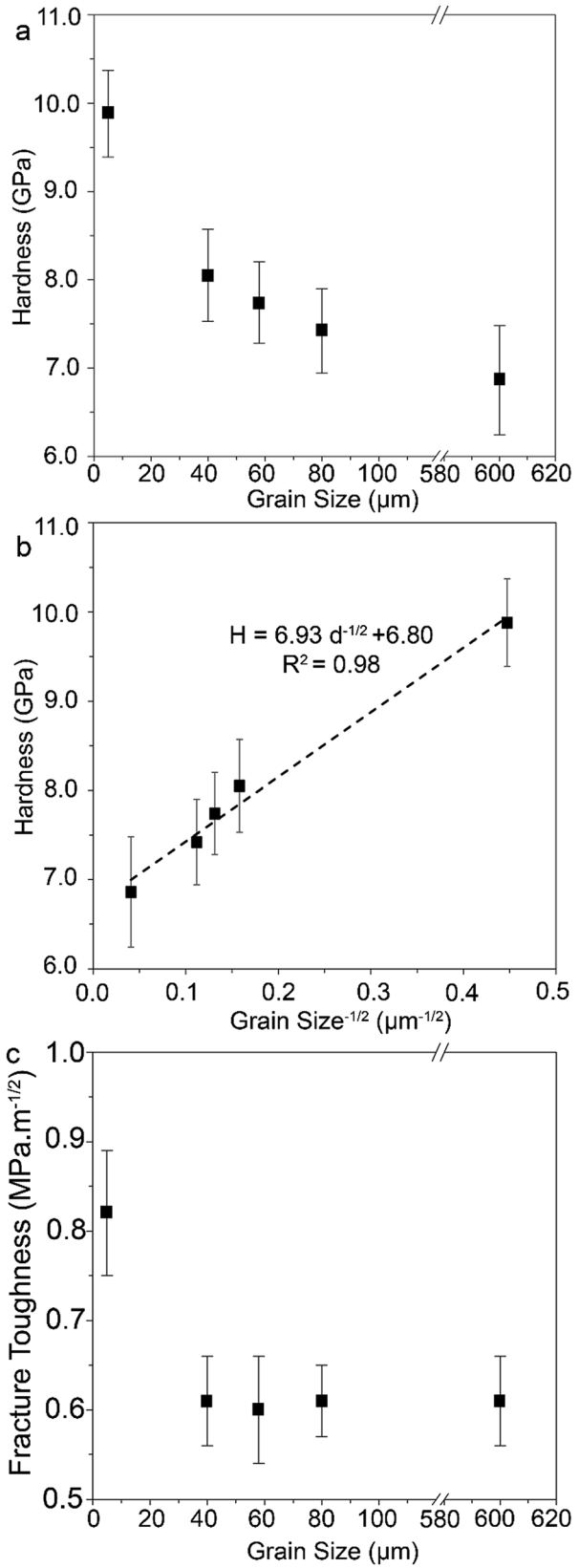

Fig. 7 Mechanical property analysis of LLZO. Vickers hardness: (a) as a function of grain size and (b) as a function of inverse square root of grain size (data follow the Hall–Petch relationship) and (c) LLZO fracture toughness as a function of grain size.

indicates that the correlation between H and grain size follows the Hall–Petch relationship. Furthermore, the LLZO single crystal H value is 6.80 GPa. The H values were used to estimate the fracture toughness as a function of grain size using eqn (2) (Experimental section).

3.3.2 Fracture toughness. The fracture toughness (K_{IC}) was measured as a function of grain size using Vickers indentation (Fig. 7c). First, it was observed that the HP-1100 °C LLZO pellet with the smallest average grain size (5 μm) has the highest fracture toughness (0.82 ± 0.07 MPa $m^{-1/2}$). This value is in good agreement with the K_{IC} value of 0.97 ± 0.10 MPa $m^{-1/2}$ for a sample of the same relative density and similar composition, but a slightly smaller grain size of ~3 μm.[54] Second, it was observed that as the average grain size increased from 5 μm to 40 μm, the fracture toughness decreased from 0.82 ± 0.07 MPa $m^{-1/2}$ to 0.60 ± 0.05 MPa $m^{-1/2}$, respectively. As the grain size further increased (≥40 μm), the fracture toughness remained relatively constant at ~0.60 MPa $m^{-1/2}$. The fracture toughness of LLZO at grain sizes greater than 40 μm is in good agreement with the results for other cubic oxides (*e.g.*, MgO).[56,57] It has been observed that the fracture toughness of cubic oxides at room temperature is relatively insensitive to grain size over the range from ~10 to 150 μm.[56,57] The increase in fracture toughness at grain sizes less than 40 μm could be related to the effect of grain boundaries on fracture toughness. In this study, indentation total crack lengths (twice the distance from the centre of the Vickers indentation to the crack tip) were typically ~25 μm. Thus, at the smaller grain size (5 μm) the grain boundary can deflect the crack resulting in an increase in fracture toughness. At grain sizes ≥40 μm the fracture toughness (0.60 ± 0.05 MPa $m^{-1/2}$) should correspond to the value for a LLZO single crystal.[24]

Using the single crystal fracture toughness value (0.60 MPa $m^{-1/2}$) and $E \sim 150$ GPa as previously reported,[25,26] also allows for estimation of the fracture surface energy (γ). γ was calculated using eqn (6):

$$\gamma = \frac{K_{IC}^2}{2E} \quad (6)$$

The fracture surface energy is estimated to be 1.24 J m^{-2}, which is in good agreement with γ values for typical single crystal ceramics (0.5–3 J m^{-2})[58] including LLZO.[54]

3.4. Electrochemical characterization

To evaluate the effect of LLZO grain size on the electrochemical stability (or CCD), a combination of DC cycling and EIS analysis was performed on Li–LLZO–Li symmetric cells (Fig. 8). After cell assembly and preconditioning, EIS was conducted and the data were fitted with an equivalent circuit (Fig. 8a) to determine the individual impedance contributions to the total cell impedance. The LLZO bulk (Z_{bulk}), grain boundary (Z_{gb}), and Li–LLZO interfacial ($Z_{Li-LLZO}$) impedances comprised the total cell impedance. A representative EIS spectrum of a cell consisting of an A-1300 °C LLZO pellet is shown in Fig. 8b. Analysis of the EIS spectrum determined that a remarkably low $Z_{Li-LLZO}$ of

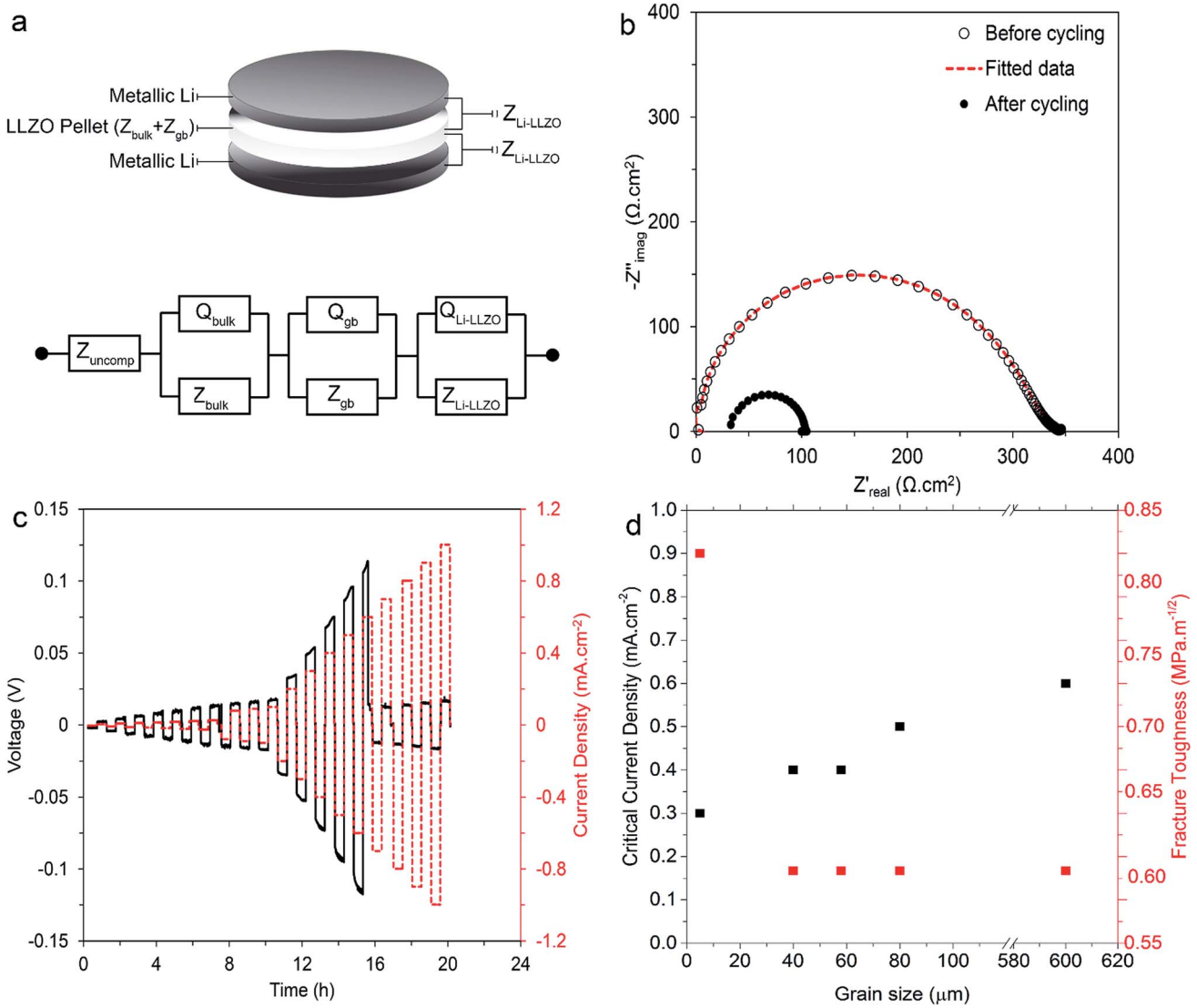

Fig. 8 AC and DC electrochemical measurements, (a) schematic diagram of the all solid-state Li–LLZO–Li cell configuration and the equivalent circuit used to model the EIS data, (b) a representative Nyquist plot of the Li–LLZO–Li cell before (○) and after (●) cycling (A-1300 °C LLZO pellet). Markers indicate experimental data and dotted lines are simulated lines extrapolated using the equivalent circuit model shown in (a), (c) DC cycling of the Li–LLZO–Li cell (A-1300 °C LLZO pellet) at room temperature, stepping the current density from 0.01 to 1 mA cm^{-2}, 30 min in each polarization orientation, and (d) the CCD and fracture toughness (taken from Fig. 7c) as a function of grain size.

2 Ω cm^{-2} was achieved using the previously reported LLZO heat-treatment prior to cell assembly.[59] It was also apparent that the LLZO total impedance ($Z_{bulk} + Z_{gb}$) was the primary contribution to the total cell impedance. The total LLZO conductivity of all the samples is listed in Table 1. From Table 1 the total conductivities are similar, except for the HP-1100 °C pellet. The LLZO total impedance was ~300 Ω cm^2, which is consistent with the values reported previously for LLZO with the same composition and high relative density.[9,10,19] All the cells had consistently low $Z_{Li-LLZO}$ (in the range of 2 to 5 Ω cm^2), eliminating the effect of Li–LLZO interfacial impedance on the CCD. Therefore, the only variable between cells was the LLZO grain size.

A representative DC cycling voltage profile of a Li–LLZO–Li symmetric cell consisting of an A-1300 °C LLZO pellet (600 ± 200 μm average grain size) is shown in Fig. 8c. The cell followed an ohmic behavior ($V = IR$) at lower current densities, but exhibited a sudden drop in polarization voltage at 0.6 mA cm^{-2}. Thus, the CCD was determined to be 0.6 mA cm^{-2}; this value is one of the highest values reported in the literature for an all solid-state Li–LLZO cell.[10,13–15,19,60–62] The EIS conducted on the cell after the CCD was exceeded (Fig. 8b), indicated a different behavior compared to previous reports on similar short-circuited symmetric cells.[10,19] As mentioned above the total cell impedance was ~300 Ω cm^2 before the CCD was exceeded; however, after the CCD was exceeded the total cell impedance (diameter of the semicircle) decreased to ~70 Ω cm^2. Additionally, the high frequency intercept no longer extended to the origin, but instead terminated on the Z_{real} axis at approximately 30 Ω cm^2. We believe that $Z_{uncompensated}$ increased based on the

equivalent circuit model fitting. The reason for the increase is not known now, but we believe it could be related to the short-circuiting phenomenon.[10,19] A similar short-circuiting behavior was observed in the other LLZO pellets in this study. More work is necessary to better interpret the EIS spectra after short-circuiting in solid-state cells containing LLZO with larger average grain size. The CCD for Li–LLZO–Li cells using LLZO pellets with average grain sizes ranging between 5 and 600 μm is shown in Fig. 8d. With increasing average grain size, the CCD increases from 0.3 to 0.6 mA cm^{-2}. These observations indicate that the LLZO CCD increases with increasing grain size. From Table 1 it should be noted that the smallest grain size of 5 μm exhibited a different value for the misorientation angle, total conductivity and fracture toughness compared to the four larger grain size samples. Thus, it is possible that not only grain size but the misorientation angle could affect the CCD. However, if this grain size is ignored the trend shown in Fig. 8d is still valid, that increasing grain size leads to a high CCD, since from Table 1 it is observed that the four larger grain size samples all exhibit similar values for the misorientation angle, total conductivity and fracture toughness, the only variable between them is grain size.

4. Discussion

Previous studies that evaluated the electrochemical stability of polycrystalline LLZO against metallic Li, observed short-circuiting when the CCD was exceeded in DC cycling tests.[10,12–14,19,63] It is generally believed that exceeding the CCD results in short-circuiting and is accompanied by Li metal filament propagation. However, little is known about the parameters that govern the CCD and the related phenomena. There have been several hypotheses proposed to determine what factors that control the CCD. Some are based on theory suggesting that mechanical properties such as the shear modulus and fracture toughness are important.[16,17] For example, Monroe *et al.* proposed that if the shear modulus of a SSE is greater than a factor of two higher than the shear modulus of Li (4.8 GPa), dendrite initiation should not occur.[16] In studies investigating the initiation and propagation of Na metal through the polycrystalline sodium beta alumina (SBA), it was determined that the CCD was affected by the fracture toughness (K_{IC}) of the SSE.[17,64] It was shown that the CCD was very sensitive to any change in the fracture toughness (K_{IC}).[4] Furthermore, in hypotheses based on experimental data, it has been suggested that microstructural features such as the grain size and/or grain boundaries influence the CCD.[11,19] For example, L. Cheng *et al.* showed that the CCD is strongly correlated with the grain size. It was shown that small grain LLZO exhibited a higher CCD compared to large grains.[11] The improved cycling behavior was attributed to the larger relative area fraction of grain boundaries at the Li–LLZO interface, which is contrary to the observations in this study. In contrast, E. J. Cheng *et al.*, using SEM and high spatial resolution Auger spectroscopy, showed that metallic Li preferentially propagates along the grain boundaries when the CCD is exceeded in hot-pressed LLZO.[19] E. J. Cheng *et al.* suggested that elimination of grain boundaries as failure points from polycrystalline LLZO could increase the CCD.[19] The purpose of this study was to correlate the effect of grain size and the resulting changes in mechanical and electrochemical properties on controlling the CCD. Table 1 summarizes the results obtained for phase purity, relative density, average grain size, mechanical properties and electrochemical properties in all LLZO pellets.

4.1. Impact of mechanical properties on CCD

Because the elastic modulus is a material intensive property, in general grain size does not affect the elastic properties such as the shear modulus.[23,55,65] Though in some cases porosity can affect the effective modulus, all samples analysed in this work had high relative densities, thus it was assumed that the elastic modulus values for the hot-pressed pellets used in this study agree with previously reported values on dense LLZO pellets.[54,57,66] For example, Ni *et al.* and others determined the shear modulus of LLZO to be 58–60 GPa, which is more than 10 times higher than the shear modulus of metallic Li.[25,26] Hence, despite meeting and exceeding the shear modulus criterion proposed by Monroe *et al.*, the DC cycling of Li–LLZO–Li symmetric cells have shown a sudden drop in polarization voltage at current densities <0.5 mA cm^{-2}, which is consistent with short-circuiting or Li metal propagation.[16] This confirms that the Monroe model is not applicable to polycrystalline LLZO. Hence, the shear modulus is not or cannot be the only parameter controlling the Li–LLZO interface stability.

Microstructural features such as the grain size, secondary phases, and porosity can affect hardness and fracture toughness.[23,32,57,67,68] In this study, it was assumed that the fraction of secondary phases and porosity were negligible and that the only microstructural feature to affect the non-elastic mechanical properties was the grain size. To evaluate effect of fracture toughness on CCD, the influence of grain size on fracture toughness was studied. The fracture toughness of LLZO decreased with increasing grain size from 5 to 40 μm and remained constant for LLZO with grain sizes ≥40 μm. This suggests that if fracture toughness was the only factor controlling the CCD, LLZO with grain sizes ≥40 μm should have exhibited a lower CCD compared to LLZO with an average grain size of 5 μm. However, the DC cycling measurements between 0.01 and 1.0 mA cm^{-2} determined that the CCD increased with increasing grain size while the fracture toughness remained constant (~0.60 MPa $m^{-1/2}$) (Fig. 8d). In fact, the CCD doubles with increasing grain size from 5 to 600 μm while the fracture toughness decreases from 0.82 ± 0.07 to 0.60 ± 0.05 MPa $m^{-1/2}$, respectively. Based on these observations, it is unlikely that there was a correlation between the fracture toughness and the CCD in this study. Moreover, we believe that mechanical properties (elastic or non-elastic) may not affect the LLZO CCD as previously believed.

4.2. Impact of grain size on CCD

The effect of grain size on the cycling behavior and the stability of LLZO against metallic Li was studied. For this purpose, the average grain size was varied over a wide range by hot-pressing between 1100 and 1300 °C and by annealing hot-pressed LLZO

at 1300 °C for 50 h. The average grain size increased from 5 ± 2 to 600 ± 200 μm. As described in Sections 2.1.1 and 2.1.2, the LLZO pellets examined here contained negligible secondary phases, were close to the theoretical density, and had consistent and low Li–LLZO interfacial impedance between 2 and 5 Ω cm^2. By controlling these material aspects, the grain size was successfully isolated as the only variable to change among the cycled LLZO pellets. Our results show that by increasing the grain size, and effectively lowering the grain boundary area per unit area of the Li–LLZO interface, an increase in CCD was achieved. The findings of this study contradict the outcomes of the study conducted by L. Cheng *et al.* who observed the opposite trend, *i.e.* the CCD increased as the grain size decreased. The improved cycling stability was attributed to the larger relative area fraction of grain boundaries at the Li–LLZO interface, which was also believed to reduce the Li–LLZO interfacial impedance.[11] For example, in the L. Cheng *et al.* study, the LLZO pellets consisting of smaller grains exhibited one-third the interfacial impedance, compared to the LLZO pellets with larger grains at the Li–LLZO interface. It is also possible that the difference in the effect of grain size on the CCD for this study and that of L. Cheng *et al.*[16] could be a result of the nature of the grain boundaries formed during hot-pressing *versus* sintering. The grain boundaries formed during hot-pressing typically exhibit increased strength compared to those formed during sintering. This may explain why the fracture mode of the hot-pressed material in this study was nearly all transgranular while the fracture mode of pressure-less sintered LLZO primarily consisted of intergranular fracture. Typically, transgranular fracture is associated with high grain boundary strength, while intergranular fracture is associated with relatively low grain boundary strength.[54] Finally, it is possible that the grain boundary chemistries were not comparable based on the different densification techniques and conditions. Altogether, due to the numerous differences in processing conditions and the impact each may have on the microstructural aspects, we believe it would be difficult to correlate the CCD behavior of the LLZO in this study and the LLZO prepared by Cheng *et al.*[16]

In related work, it has been shown that the CCD was inversely correlated with the Li–LLZO interfacial impedance; the lower the interfacial impedance, the higher the CCD.[10] Owing to its possible influence on the CCD, the interfacial impedance was not a variable in this work, suggesting that the effect of grain size was isolated. The correlation between grain size and CCD in this study is consistent with the findings reported by E. J. Cheng *et al.* who observed Li metal propagation along grain boundaries when the CCD was exceeded in Li–LLZO–Li cells.[19] It follows that if grain boundaries are initiation points for Li metal propagation into LLZO, the lower the relative area/volume fraction of grain boundaries, the less likely the Li metal propagation will occur. It could be argued that increasing the grain size would increase the current density through the grain boundaries, thereby decreasing the effective CCD; however, the results of this study suggest that the opposite is true; *i.e.* the CCD increases with increasing grain size. The results of this study suggest that increasing the CCD of LLZO can be achieved by increasing the grain size or minimizing or altogether eliminating grain boundaries (single crystal).

We believe that the outcomes of this work could have both broad scientific and practical implications. First, ostensibly, it has been believed that the CCD of LLZO should be governed by the same or similar mechanical property phenomena that control the stability of related SSE models or systems.[18–20] However, perhaps due to differences in material property assumptions, some existing hypotheses used to predict the CCD may not be consistent with the observations made in this work, *i.e.* the Monroe model is predicated on the uniform ionic conductor, while LLZO conducts ions through the bulk and grain boundaries.[18] Moreover, the findings from this and other recent work indicate that the mechanical properties of LLZO may not affect the CCD as previously suggested. Instead, these findings may point to other phenomena that have more profound effects in governing the CCD that are yet to be discovered. Clearly, more in depth studies are needed to better understand what triggers Li metal propagation in LLZO. Second, the highest room temperature CCD (0.6 mA cm^{-2}) was demonstrated with 600 μm average grain size LLZO. Taken together, our study correlates the effect of LLZO grain size and the Li–LLZO stability as a function of Li plating rate. By controlling the microstructure, a straightforward pathway towards viable solid-state batteries can be achieved.

5. Conclusions

Achieving current densities ≥1 mA cm^{-2} is a necessary condition for a viable solid-state electrolyte to enable the use of metallic Li anodes. Toward this goal, the present study has examined parameters such as fracture toughness and grain size that could affect the maximum tolerable current density. It was observed that maximum current density was roughly independent of fracture toughness and strongly dependent on grain size. When the grain size increased from 5 to 600 μm the CCD increased from 0.3 to 0.6 mA cm^{-2}, respectively. It is believed that this increase in grain size reduced the grain boundary area and hence the number of possible failure points leading to an increased CCD. These results indicate that further efforts should be focused on the elimination of grain boundaries from the microstructure to suppress Li filament propagations in polycrystalline SSEs and allow for improvements of solid-state battery technology.

Conflicts of interest

There are no conflicts to declare.

Acknowledgements

A. S., C. G. H., J. W., and J. S. would like to acknowledge support from the U.S. Department of Energy (DOE), Office of Energy Efficiency and Renewable Energy (EERE), Vehicle Technologies Office (VTO) and Advanced Battery Materials Research (BMR) program under contract DE-EE 00006821. J. W. would like to acknowledge support of the Army Research Laboratory.

References

1 R. Van Noorden, *Nature*, 2014, **507**, 26–28.
2 P. G. Bruce, S. A. Freunberger, L. J. Hardwick and J.-M. Tarascon, *Nat. Mater.*, 2012, **11**, 19–29.
3 J. Sakamoto, *Handbook of Solid State Batteries*, 2015, vol. 6, p. 391.
4 R. Murugan, V. Thangadurai and W. Weppner, *Angew. Chem., Int. Ed.*, 2007, **46**, 7778–7781.
5 S. Stramare, V. Thangadurai and W. Weppner, *Chem. Mater.*, 2003, **15**, 3974–3990.
6 V. Thangadurai, H. Kaack and W. J. Weppner, *J. Am. Ceram. Soc.*, 2003, **86**, 437–440.
7 V. Thangadurai and W. Weppner, *Ionics*, 2006, **12**, 81–92.
8 T. Thompson, S. Yu, L. Williams, R. D. Schmidt, R. Garcia-Mendez, J. Wolfenstine, J. L. Allen, E. Kioupakis, D. J. Siegel and J. Sakamoto, *ACS Energy Lett.*, 2017, **2**, 462–468.
9 Y. Kim, A. Yoo, R. Schmidt, A. Sharafi, H. Lee, J. Wolfenstine and J. Sakamoto, *Frontiers in Energy Research*, 2016, **4**, 1–7.
10 A. Sharafi, H. M. Meyer, J. Nanda, J. Wolfenstine and J. Sakamoto, *J. Power Sources*, 2016, **302**, 135–139.
11 L. Cheng, C. H. Wu, A. Jarry, W. Chen, Y. Ye, J. Zhu, R. Kostecki, K. Persson, J. Guo and M. Salmeron, *ACS Appl. Mater. Interfaces*, 2015, **7**, 17649–17655.
12 K. Ishiguro, Y. Nakata, M. Matsui, I. Uechi, Y. Takeda, O. Yamamoto and N. Imanishi, *J. Electrochem. Soc.*, 2013, **160**, A1690–A1693.
13 R. Sudo, Y. Nakata, K. Ishiguro, M. Matsui, A. Hirano, Y. Takeda, O. Yamamoto and N. Imanishi, *Solid State Ionics*, 2014, **262**, 151–154.
14 S. Ohta, T. Kobayashi, J. Seki and T. Asaoka, *J. Power Sources*, 2012, **202**, 332–335.
15 L. Cheng, J. S. Park, H. Hou, V. Zorba, G. Chen, T. Richardson, J. Cabana, R. Russo and M. Doeff, *J.Mater. Chem. A*, 2014, **2**, 172–181.
16 C. Monroe and J. Newman, *J. Electrochem. Soc.*, 2005, **152**, A396–A404.
17 A. V. Virkar and G. R. Miller, *J. Mater. Sci.*, 1983, **18**, 1202–1212.
18 A. V. Virkar, L. Viswanathan and D. R. Biswas, *J. Mater. Sci.*, 1980, **15**, 302–308.
19 E. J. Cheng, A. Sharafi and J. Sakamoto, *Electrochim. Acta*, 2017, **223**, 85–91.
20 E. Rangasamy, J. Wolfenstine and J. Sakamoto, *Solid State Ionics*, 2012, **206**, 28–32.
21 M. Harmer and R. Brook, *Trans. J. Br. Ceram. Soc.*, 1981, **80**, 147–148.
22 I. N. David, T. Thompson, J. Wolfenstine, J. L. Allen and J. Sakamoto, *J. Am. Ceram. Soc.*, 2015, **98**, 1209–1214.
23 W. D. Callister and D. G. Rethwisch, *Mater. Sci. Engin*, John Wiley & Sons, NY, 2011.
24 G. Anstis, P. Chantikul, B. R. Lawn and D. Marshall, *J. Am. Ceram. Soc.*, 1981, **64**, 533–538.
25 J. E. Ni, E. D. Case, J. S. Sakamoto, E. Rangasamy and J. B. Wolfenstine, *J. Mater. Sci.*, 2012, **47**, 7978–7985.
26 S. Yu, R. D. Schmidt, R. Garcia-Mendez, E. Herbert, N. J. Dudney, J. B. Wolfenstine, J. Sakamoto and D. J. Siegel, *Chem. Mater.*, 2015, **28**, 197–206.
27 J. T. Irvine, D. C. Sinclair and A. R. West, *Adv. Mater.*, 1990, **2**, 132–138.
28 R. A. Huggins, *Ionics*, 2002, **8**, 300–313.
29 M. Huang, T. Liu, Y. Deng, H. Geng, Y. Shen, Y. Lin and C.-W. Nan, *Solid State Ionics*, 2011, **204**, 41–45.
30 J. A. Wollmershauser, B. N. Feigelson, E. P. Gorzkowski, C. T. Ellis, R. Goswami, S. B. Qadri, J. G. Tischler, F. J. Kub and R. K. Everett, *Acta Mater.*, 2014, **69**, 9–16.
31 A. Goldstein, *J. Eur. Ceram. Soc.*, 2012, **32**, 2869–2886.
32 W. Barsoum, *Fundamentals of Ceramics*, Taylor & Francis, 2002.
33 D. W. Richerson, *Modern Ceramic Engineering: Properties, Processing, and Use in Design*, CRC press, 2005.
34 W. Wang, Z. Fu, H. Wang and R. Yuan, *J. Eur. Ceram. Soc.*, 2002, **22**, 1045–1049.
35 A. Daniels, R. Lowrie, R. Gibby and I. B. Cutler, *J. Am. Ceram. Soc.*, 1962, **45**, 282–285.
36 R. Spriggs, L. Brissette and T. Vasilos, *J. Am. Ceram. Soc.*, 1964, **47**, 417–418.
37 D. Turnbull, *J. Met.*, 1951, **3**, 661–665.
38 R. Brook, *Scr. Metall.*, 1968, **2**, 375–378.
39 R. L. Coble, *J. Appl. Phys.*, 1961, **32**, 793–799.
40 J. Wolfenstine, J. Sakamoto and J. Allen, *J. Mater. Sci.*, 2012, **47**, 4428–4431.
41 R. S. Gordon, *J. Am. Ceram. Soc.*, 1973, **56**, 147–152.
42 A. Ruoff, *J. Appl. Phys.*, 1965, **36**, 2903–2907.
43 D. Cherniak, *Phys. Chem. Miner.*, 1998, **26**, 156–163.
44 L. C. De Jonghe and M. N. Rahaman, *Handbook of Advanced Ceramics: Materials, Applications, Processing and Properties*, 2003, vol. 2, p. 187.
45 M. N. Rahaman, *Sintering of Ceramics*, CRC press, 2007.
46 C. S. Barrett, *Trans. Metall. Soc. AIME*, 1940, **137**, 128–149.
47 D. J. Jensen, *Acta Metall. Mater.*, 1995, **43**, 4117–4129.
48 H. Gleiter, *Acta Metall.*, 1969, **17**, 853–862.
49 P. A. Beck, P. R. Sperry and H. Hu, *J. Appl. Phys.*, 1950, **21**, 420–425.
50 M. Parthasarathi and P. A. Beck, *Trans. Metall. Soc. AIME*, 1961, **221**, 831–838.
51 H. Yoshida, B. Liebmann and K. Lücke, *Acta Metall.*, 1959, **7**, 51–56.
52 A. S. f. Metals, *Recrystallization, grain growth, and textures: papers presented at a seminar of the American Society for Metals, October 16 and 17, 1965*, American Society for Metals, 1966.
53 S. Kohara, M. Parthasarathi and P. A. Beck, *J. Appl. Phys.*, 1958, **29**, 1125–1126.
54 Y. Kim, H. Jo, J. L. Allen, H. Choe, J. Wolfenstine and J. Sakamoto, *J. Am. Ceram. Soc.*, 2016, **99**, 1367–1374.
55 J. B. Wachtman, W. R. Cannon and M. J. Matthewson, in *Mechanical Properties of Ceramics*, John Wiley & Sons, Inc., 2009, pp. 27–33, DOI: 10.1002/9780470451519.ch2.
56 R. W. Rice, S. W. Freiman and P. F. Becher, *J. Am. Ceram. Soc.*, 1981, **64**, 345–350.
57 R. Rice, *J. Mater. Sci.*, 1996, **31**, 1969–1983.

58 R. W. Davidge, *Mechanical Behaviour of Ceramics*, CUP Archive, 1979, pp. 13475–13487.
59 A. Sharafi, S. Yu, M. Naguib, M. Lee, C. Ma, H. M. Meyer, M. Chi, J. Nanda, D. J. Siegel and J. Sakamoto, *J. Mater. Chem. A*, 2017, **5**, 13475.
60 H. Buschmann, J. Dölle, S. Berendts, A. Kuhn, P. Bottke, M. Wilkening, P. Heitjans, A. Senyshyn, H. Ehrenberg and A. Lotnyk, *Phys. Chem. Chem. Phys.*, 2011, **13**, 19378–19392.
61 K. Ishiguro, H. Nemori, S. Sunahiro, Y. Nakata, R. Sudo, M. Matsui, Y. Takeda, O. Yamamoto and N. Imanishi, *J. Electrochem. Soc.*, 2014, **161**, A668–A674.
62 X. Han, Y. Gong, K. K. Fu, X. He, G. T. Hitz, J. Dai, A. Pearse, B. Liu, H. Wang, G. Rubloff, Y. Mo, V. Thangadurai, E. D. Wachsman and L. Hu, *Nat. Mater.*, 2016, **5**, 572–579.
63 Y. Ren, Y. Shen, Y. Lin and C.-W. Nan, *Electrochem. Commun.*, 2015, **57**, 27–30.
64 A. V. Virkar and L. Viswanathan, *J. Mater. Sci.*, 1983, **18**, 1202–1212.
65 R. F. Cook, B. R. Lawn and C. J. Fairbanks, *J. Am. Ceram. Soc.*, 1985, **68**, 604–615.
66 H. Chou and E. D. Case, *J. Mater. Sci. Lett.*, 1988, **7**, 1217–1220.
67 D. Shahriari, J. Y. Koffler, M. H. Tuszynski, W. M. Campana and J. S. Sakamoto, *Tissue Eng., Part A*, 2017, **23**, 415–425.
68 R. Rice, *J. Mater. Sci.*, 1996, **31**, 4503–4519.

